



## Electronic structure, optical and sonophotocatalytic properties of spindle-like $\text{CaWO}_4$ microcrystals synthesized by the sonochemical method



P.B. de Sousa <sup>a</sup>, A.F. Gouveia <sup>b</sup>, J.C. Sczancoski <sup>c</sup>, I.C. Nogueira <sup>d</sup>, E. Longo <sup>c</sup>,  
M.A. San-Miguel <sup>b</sup>, L.S. Cavalcante <sup>a, e,\*</sup>

<sup>a</sup> Universidade Federal do Piauí, Campus Ministro Petrônio Portella, Ininga, 64049-550, Teresina-PI, Brazil

<sup>b</sup> Institute of Chemistry, State University of Campinas, 13083-970, Campinas, São Paulo, Brazil

<sup>c</sup> DEMA-DQ-Universidade Federal de São Carlos, P.O. Box 676, São Carlos, SP, 13565-905, Brazil

<sup>d</sup> Universidade Federal do Amazonas, Av. Rodrigo Otávio Japiim, P.O. Box 670, 69077-000, Manaus-AM, Brazil

<sup>e</sup> Universidade Estadual do Piauí, Rua João Cabral, N. 2231, P.O. Box 381, 64002-150, Teresina-PI, Brazil

### ARTICLE INFO

#### Article history:

Received 6 July 2020

Received in revised form

7 September 2020

Accepted 27 September 2020

Available online 28 September 2020

#### Keywords:

$\text{CaWO}_4$  crystals

Optical band gap

Band structure

Sonophotocatalysis properties

### ABSTRACT

In this letter, the electronic structure, optical, and sonophotocatalytic properties of calcium tungstate ( $\text{CaWO}_4$ ) microcrystals synthesized by the sonochemical method are reported. Structural and morphological characterization techniques revealed that  $\text{CaWO}_4$  has a tetragonal structure and composed of several spindle-like microcrystals. The ultraviolet-visible spectroscopy showed an optical band gap energy  $E_{\text{gap(exp)}}$  of 4.69 eV. The theoretical calculations were performed to describe the electronic band structure, the density of states, and Infrared/Raman vibrational modes. The theoretical models were based on optimized and defect-based structures. The theoretical optical band gap energy ( $E_{\text{gap}}$ ) confirmed the existence of direct electronic transitions ( $\Gamma \leftrightarrow \Gamma$  points in Brillouin zone). The optimized structure exhibited an  $E_{\text{gap(theo)}}$  value of 5.70 eV due to the participation of energy levels arising from O and Ca atoms in the valence band as well as W and O atoms in the conduction band. A decrease from 5.70 to 4.29 eV was observed for the defect-based structure. The sonophotocatalytic properties of  $\text{CaWO}_4$  microcrystals were investigated for the first time with respect to degradation of Rhodamine B dye and they revealed a degradation capacity of approximately 96% after 200 min. Finally, our electron density maps indicate that the presence of structural defects induces a polarization phenomenon and inhomogeneous distribution of electron charge between the  $[\text{CaO}_8]-[\text{WO}_4]$  clusters.

© 2020 Elsevier B.V. All rights reserved.

### 1. Introduction

The tungstates are inorganic oxides formed by divalent metal cation with general formula  $\text{AWO}_4$  (where  $\text{A}^{2+}$  are Ca, Sr, Ba, Pb and Cd). Among these, the calcium tungstate ( $\text{CaWO}_4$ ) is the most important compound at group of the scheelites, a specific tetragonal structure with space group ( $I4_1/a$ ), possessing four molecular formula per unit cell ( $Z = 4$ ) in which the W atoms are coordinated to four equivalent O atoms, forming tetrahedral  $[\text{WO}_4]$  clusters isolated from each other, while the Ca atoms are coordinated to eight O atoms, forming the deltraedra  $[\text{CaO}_8]$  clusters [1,2]. Such oxide materials have been extensively studied and found numerous

technological and socio-environmental application possibilities, due to their interesting luminescent and structural peculiarities [3], such as diode lasers [4], scintillators [5], fluorescent lamps [6], drug carrier [7], temperature sensing [8] and catalysts [9].

In recent years,  $\text{CaWO}_4$  crystals with different sizes and shapes have been prepared by a wide variety of synthesis methods, including radio-frequency sputtering [10], sol-gel [11], hydrothermal [7], solid state reaction [12], co-precipitation [13], polymeric precursor [14], solvothermal [15], microwave assisted synthesis [16], electrospinning [6], and pulse laser ablation [17]. However, among the previously mentioned methods, the sonochemical (SC) method has been shown to be more efficient due to its simplicity and low cost, resulting in products with high purity and crystallinity, dispensing long periods of synthesis, high temperatures and pressures or special equipment, conditions not suitable for large scale productions or industrial applications [2,18]. The SC method is based on the acoustic cavitation phenomenon, which consists in

\* Corresponding author. Universidade Federal do Piauí, Campus Ministro Petrônio Portella, Ininga, 64049-550, Teresina-PI, Brazil.

E-mail address: [laeciosc@gmail.com](mailto:laeciosc@gmail.com) (L.S. Cavalcante).

the formation, growth and implosive collapse of vapor bubbles in a liquid, in a cycle that lasts throughout the period of ultrasonic irradiation [19]. Immediately after the collapse of the cavitation bubbles, the so-called "hot spots" (microscopically located liquid regions that have high temperatures and pressures: 5000 K and 1000 atm, approximately) are generated, capable of significantly increasing the chemical reactions rates [20,21], a fact by which the ultrasound has also been used as an aid in organic pollutants degradation processes [22].

Therefore, this letter reports the synthesis of spindle-like CaWO<sub>4</sub> microcrystals by the SC method and the evaluation of its sonophotocatalytic (SPC) activity in the degradation of Rhodamine B (RhB) dye under UV-C illumination. These CaWO<sub>4</sub> microcrystals were characterized by X-ray diffraction (XRD), Rietveld refinement, micro-Raman, Fourier transform-infrared (FT-IR) and ultraviolet-visible (UV-Vis) spectroscopies. The morphology aspects and elemental composition analysis were investigated by field emission-scanning electron microscopy (FE-SEM) and energy-dispersive X-ray spectrometry (EDXS), respectively. In addition, we report on first-principles quantum mechanical calculations based on density functional theory (DFT) the electronic band structure (EBS), density of states (DOS), infrared/Raman vibrational modes and electronic density map to better explain the experimental results. For the first time, the enhanced SPC properties of spindle-like CaWO<sub>4</sub> microcrystals for the degradation of RhB under UV-C illumination were described in detail.

## 2. Experimental details

### 2.1. Synthesis of CaWO<sub>4</sub> crystals

CaWO<sub>4</sub> microcrystals were synthesized by the SC method described as follows:  $1.0 \times 10^{-3}$  mol of sodium tungstate (VI) dihydrate ( $\text{Na}_2\text{WO}_4 \cdot 2\text{H}_2\text{O}$ ; 99.0% purity, Sigma-Aldrich) and  $1.0 \times 10^{-3}$  mol of calcium nitrate tetrahydrate [ $\text{Ca}(\text{NO}_3)_2 \cdot 4\text{H}_2\text{O}$ ; 99% purity, Sigma-Aldrich] were separately placed in two Falcon tubes (capacity of 50 mL) and dissolved in 50 mL of deionized water (DI-H<sub>2</sub>O) at room temperature. The solution containing  $\text{WO}_4^{2-}$  complex anion was transferred to a graduated borosilicate reagent bottle of 100 mL, partially immersed in an ultrasonic bath (Bransonic CPX1800H Digital) operating at 40 kHz and 70 W. Then the solution containing the Ca<sup>2+</sup> ions was slowly dripped (one drop per second, approximately), with the aid of a graduated burette, into of the Borosilicate bottle containing the  $\text{WO}_4^{2-}$  ions. At the end of the drip, the system was maintained at 40 °C for 3 h under sonication. The theoretical calculation of the total-energy to study the electronic structure and optical properties of CaWO<sub>4</sub> crystals was performed with the CRYSTAL17 software package [23,24] and the methodology is based on the DFT associated with the hybrid functional B3PYP [25,26] (See Supplementary data for more details about Synthesis, characterizations, sonophotocatalytic measurements, theoretical calculations and average size distribution).

## 3. Results and discussions

### 3.1. Structural analysis: Experimental and theoretical

XRD patterns, micro-Raman and FT-IR spectra of spindle-like CaWO<sub>4</sub> microcrystals synthesized by the SC method are shown in Fig. 1(a–c). Fig. 1(d and e) display the comparison between the relative positions of theoretical and experimental Raman and IR-active modes, respectively.

The diffraction patterns shown in Fig. 1(a) indicate that the CaWO<sub>4</sub> sample have a scheelite-type tetragonal structure with

space group ( $I4_1/a$ ) and point-group symmetry ( $C_{4h}^6$ ) being in agreement with the Inorganic Crystal Structure Database (ICSD) file no. 60547 [27]. No deleterious or intermediate phase was detected. Moreover, detected sharp and well-defined diffraction peaks indicate a high degree of structural order and periodicity of the CaWO<sub>4</sub> crystalline lattice at long-range [28]. Fig SI-1 illustrate the Rietveld refinement plots for the CaWO<sub>4</sub> microcrystals with observed patterns versus the calculated patterns. Moreover, the profiles of XRD patterns experimentally observed and theoretically calculated display small differences between the observed  $y$ -scale values ( $Y_{\text{Obs}}$ ) and calculated  $y$ -values ( $Y_{\text{Calc}}$ ) on the intensity scale near zero, as illustrated by the ( $Y_{\text{Obs}} - Y_{\text{Calc}}$ ) line. Tables SD-1 presents the fit parameters ( $R_{\text{wp}}$ ,  $R_p$ ,  $R_{\text{Bragg}}$ ,  $\chi^2$  and  $S$ ), which suggest that the refinement results are very reliable (Supplementary data Figs. SD-1). In Fig. 1(b), we detect eleven Raman-active vibrational modes, the  $A_g$  mode at 911 cm<sup>-1</sup> is assigned to the ( $\leftarrow \text{O} \leftarrow \text{W} \rightarrow \text{O} \rightarrow$ ) symmetric stretching vibrations within the tetrahedral [WO<sub>4</sub>] clusters, while the  $B_g$  mode located at 836 cm<sup>-1</sup> and the  $E_g$  mode located at 797 cm<sup>-1</sup> are ascribed to the ( $\leftarrow \text{O} \leftarrow \text{W} \leftarrow \text{O} \leftarrow$ )/( $\rightarrow \text{O} \rightarrow \text{W} \rightarrow \text{O} \rightarrow$ ) anti-symmetric stretching vibrations. The  $B_g$  mode located at 399 cm<sup>-1</sup> and the  $A_g$  and  $B_g$  modes located both at 332 cm<sup>-1</sup> are associated, respectively, to the anti-symmetric and symmetric bending vibration in the tetrahedral [WO<sub>4</sub>] clusters. The Raman shift due to the free rotation of tetrahedral [WO<sub>4</sub>] clusters is noted at 209 cm<sup>-1</sup> and 194 cm<sup>-1</sup> referring to  $E_g$  and  $B_g$  modes, respectively. The  $E_g$  mode at 115 cm<sup>-1</sup> ( $E_g$ ) is assigned to free motion at ( $x$ ,  $y$ ,  $z$ -axis) of the deltahedral [CaO<sub>8</sub>] clusters [28]. Finally, the Raman-active  $B_g$  mode at 86 cm<sup>-1</sup> is related to symmetric bending vibrations of (O–Ca–O) bonds in deltahedral [CaO<sub>8</sub>] clusters [9,30,31]. Fig. 1(c) presents the FT-IR spectrum, which depicts only three of eight possible IR-active modes were verified. These three IR-active vibrational modes were identified for our CaWO<sub>4</sub> crystals exhibited an overlapping of two intense absorption bands [ $v_3(1E_u$  and  $1A_u)$ ] in the range from 794 cm<sup>-1</sup> to 854 cm<sup>-1</sup>, which were ascribed to the ( $\leftarrow \text{O} \leftarrow \text{W} \leftarrow \text{O} \leftarrow$ )/( $\rightarrow \text{O} \rightarrow \text{W} \rightarrow \text{O} \rightarrow$ ) anti-symmetric stretching vibrations within the tetrahedral [WO<sub>4</sub>] clusters (Fig. 3(d)). The  $v_4[1(A_u)]$  modes located at approximately 438 cm<sup>-1</sup> are ascribed to symmetric bending vibrations within the tetrahedral [WO<sub>4</sub>] clusters [29].

### 3.2. Optical analysis: Experimental and theoretical

The experimental optical band gap energy [ $E_{\text{gap(exp)}}$ ] of CaWO<sub>4</sub> crystals was estimated by the modified Kubelka-Munk [32] equation (1):

$$[F(R_\infty)h\nu] = C_1(h\nu - E_{\text{gap}})^n \quad (1)$$

where  $F(R_\infty)$  is the Kubelka-Munk function or absolute reflectance of the sample,  $R_\infty$  is the reflectance when the sample is infinitely thick,  $h\nu$  is the photon energy,  $C_1$  is a proportionality constant,  $E_{\text{gap}}$  is the optical band gap and  $n$  is a constant associated with different types of electronic transitions ( $n = 0.5$  and  $n = 2$  for direct and indirect allowed transitions;  $n = 1.5$  and  $n = 3$  for direct and indirect forbidden transitions, respectively). Since barium sulfate (BaSO<sub>4</sub>) was the standard sample in reflectance measurements:  $R_\infty = R_{\text{sample}}/R_{\text{standard}} = R_{\text{sample}}/R_{\text{BaSO}_4}$  [33,34]. For our CaWO<sub>4</sub> microcrystals, the theoretical calculations shown in this work indicate an optical diffuse reflectance spectra governed by direct electronic transitions, in agreement with other theoretical studies [34,35] i.e. after the photon absorption process, the electrons located in the valence band (VB), when excited to the conduction band (CB), do so under the same point in the Brillouin zone [36]. Thus, using  $n = 0.5$  in equation (1) and plotting the graph of  $[F(R_\infty)h\nu]^2$  against  $h\nu$ , it is

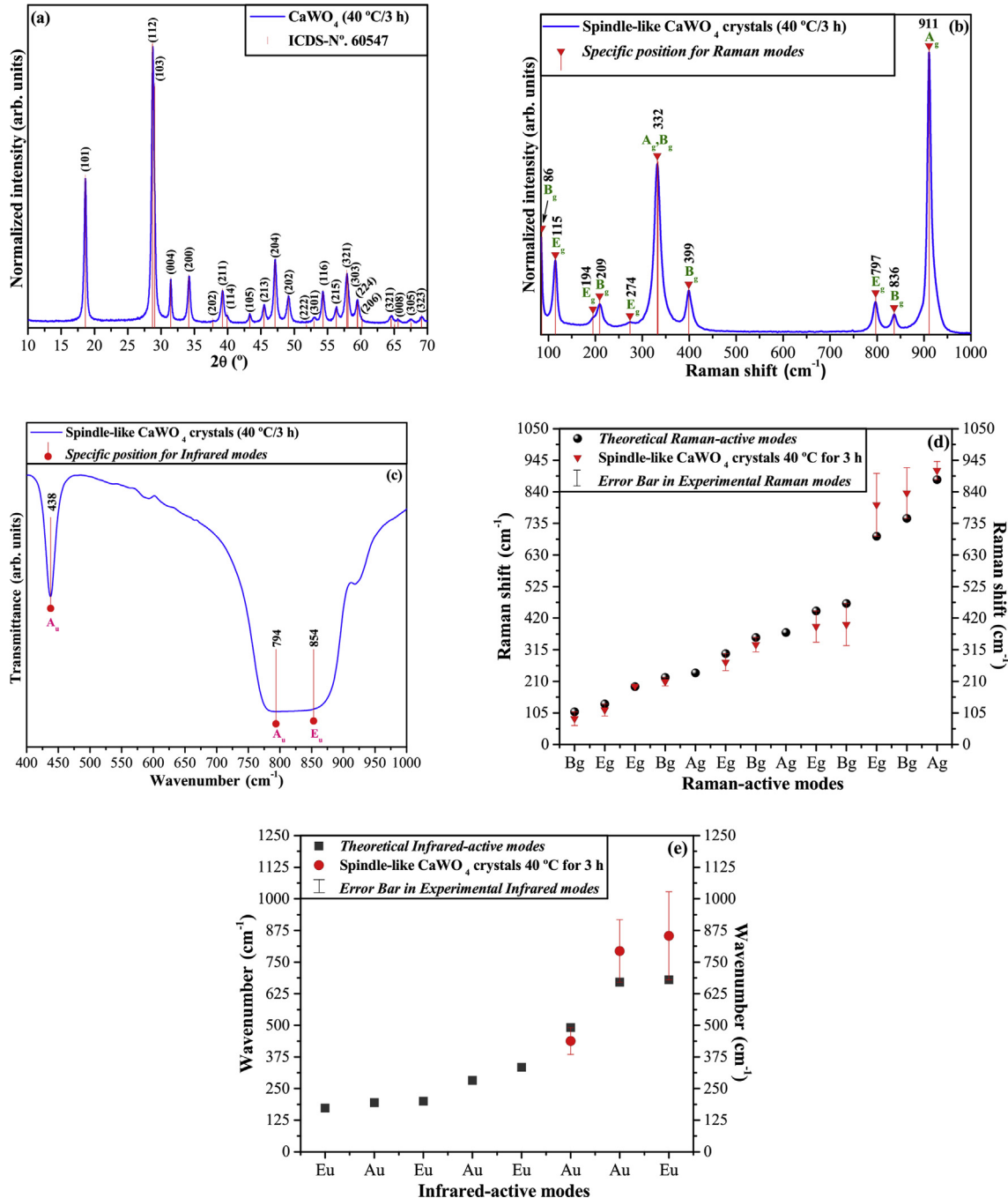


**Fig. 1.** (a) XRD patterns, (b) micro-Raman spectrum, and (c) FT-IR spectrum for  $\text{CaWO}_4$  crystals synthesized by the SC method. The vertical lines () in red color in Fig. 1(a) indicate the position and relative intensity of XRD patterns for the  $\text{CaWO}_4$  phase reported in ICSD file No. 60547. (e,d) Relative positions of experimental and theoretical Raman and IR-active modes. The error bars in the experimental Raman and IR-modes indicate the difference between the theoretical Raman and IR modes obtained by DFT calculations, respectively.

possible to estimate the  $E_{\text{gap}}$  values of the  $\text{CaWO}_4$  microcrystals by extrapolation of linear portion of the UV–Vis curve of the resulting graph to the  $y$ -axis intercept [33].

Fig. 2(a) shows the UV–Vis diffuse reflectance spectrum of  $\text{CaWO}_4$  microcrystals and its optical band gap estimated ( $E_{\text{gap(exp)}}$ ). Fig. 2(b and c) display the optimized and defected EBS of  $\text{CaWO}_4$  microcrystals and Fig. 2(d) shows DOS for optimized and defected theoretical models projected over all atoms involved in the electronic structure of the  $\text{CaWO}_4$  microcrystals.

Fig. 2(a) indicates that the UV–Vis spectrum of our  $\text{CaWO}_4$  microcrystals is characterized by well defined direct electronic

transitions with a quasi-vertical absorption profile typical of semiconductor crystalline materials [37] with a value of  $E_{\text{gap(exp)}} = 4.69$  eV. The literature [38,39] reports that  $\text{CaWO}_4$  crystals exhibit different optical band gap values ranging from 4.0 to 5.89 eV all ascribed to a direct optical band gap, suggesting that our  $E_{\text{gap(exp)}}$  value of the  $\text{CaWO}_4$  crystals synthesized by SC method and reported in this study is within acceptable values. Considering the theoretical calculations, the optimized electronic band structure of  $\text{CaWO}_4$  microcrystals is characterized by direct electronic transitions between the valence band (VB) and conduction band (CB) ( $\Gamma \leftrightarrow \Gamma$  points in the Brillouin zone) and  $E_{\text{gap(theo)}} = 5.70$  eV

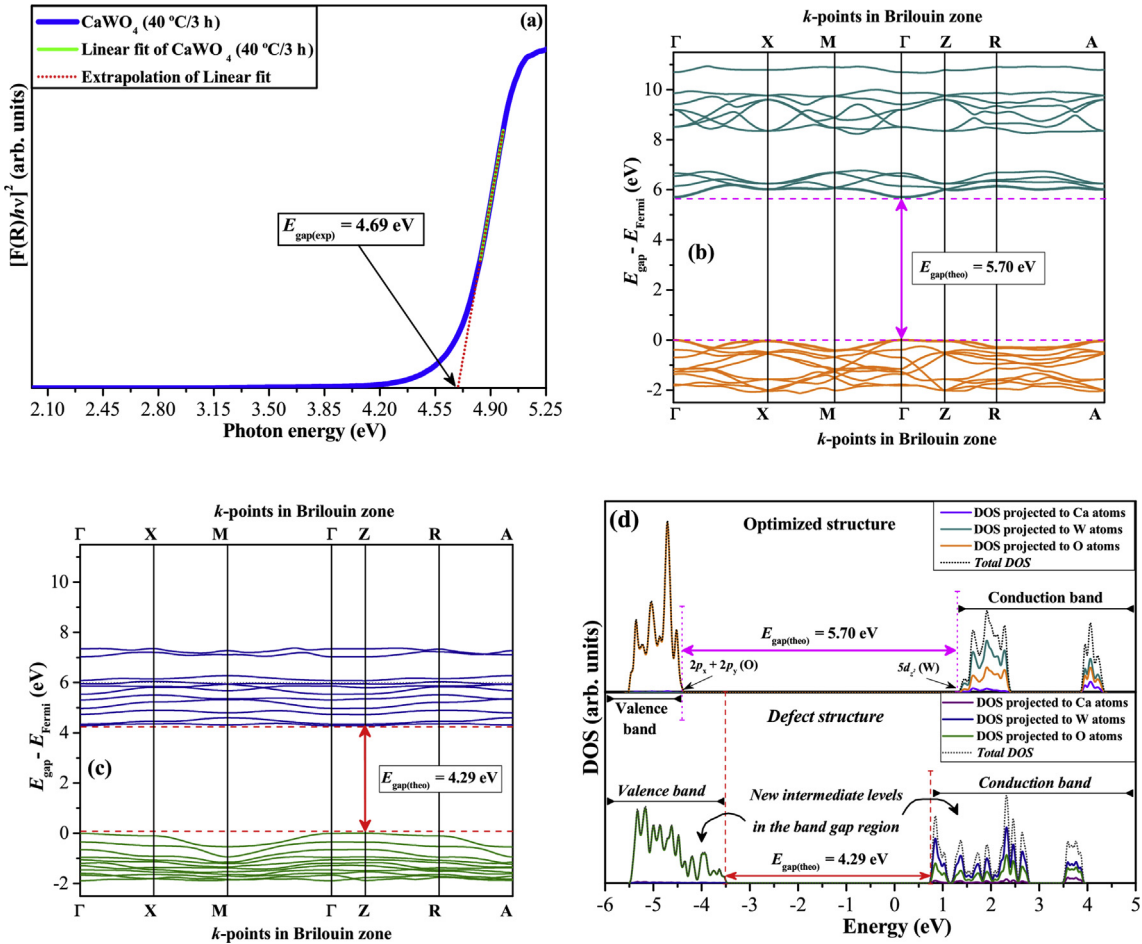


**Fig. 2.** (a) UV–Vis spectrum of  $\text{CaWO}_4$  microcrystals synthesized by the SC method, (b) optimized EBS, (c) defected EBS, and (d) Total DOS for the optimized structure and defected structure projected on the Ca, W, and O atoms of  $\text{CaWO}_4$  microcrystals, respectively.

(Fig. 2(b)). This value is higher than the experimental value because in the theoretical calculations the system is in the ideal arrangement without local defects, like distortion in the angles and bonds distances. The  $E_{\text{gap}}$  values are controlled by the degree of structural organization of the crystalline lattice: the greater the structural organization, i.e. crystallinity, the greater the value of  $E_{\text{gap}}$  [38]. The reduction of the band gap value due to the structural defects that generated energy levels between the VB and CB. In order to investigated this effect on the electronic properties, the defect model was proposed with a distortion in the O atom that is shared between the two  $[\text{CaO}_8]$  and  $[\text{WO}_4]$  clusters. As can be seen in Fig. 2(c), the local defect on the O atom induced the creation of new intermediate levels between the VB and the CB, which caused the reduction of the band gap value from  $E_{\text{gap}(\text{theo})} = 5.70 \text{ eV}$  to  $E_{\text{gap}(\text{theo})} = 4.29 \text{ eV}$ .

The study of the energy levels in the VB and CB can be better evaluated by the analysis of the DOS, as shown in Fig. 2(d). From the analysis of the DOS, it is possible to known which orbitals are involved in each band, VB and CB, in the electronic transitions and also which atoms are in the band gap region. Fig. 2(d) shows that projected total DOS for both models, optimized and defected structures, illustrate that O  $2p$  states are principal contributors to the VB and with minor input from the electronic states associated with Ca atoms, while the CB is mainly determined by W  $5d$  states with minor contributions of the unoccupied electronic states originated from O and Ca atoms. Meanwhile, the same feature

regarding O  $2p$  states in the VB, while unoccupied W  $5d$  states at the bottom of the CB was found to be characteristic of other tungstates, in particular,  $\text{CuWO}_4$ ,  $\text{FeWO}_4$ ,  $\text{CoWO}_4$ , and  $\text{ZnWO}_4$  crystals [40–43].

The O  $2p$  orbitals in the VB are mainly antibonding and the W  $5d$  orbitals in the CB are bonding and antibonding. Focusing on the electronic density near the band edges, the top of VB is predominantly composed of the O  $2p_x$  and O  $2p_y$  orbitals, whereas the bottom of the CB is formed by 4s from Ca atoms and  $5d_z^2$  orbitals from W atoms. From this result, it is possible to affirm that the atomic orbitals of all atoms in the  $\text{CaWO}_4$  structure were not degenerated, with distinct energies. Projected DOS of the  $\text{CaWO}_4$  defect structure (bottom part of Fig. 2(d)) allows observation of the new intermediate energy levels created by the disorder provoked by the defect on the O atom mainly on the VB, where the contribution of the O atoms is major. The CB also was affected due to the disorder in the  $[\text{WO}_4]$  clusters with new energy levels in this region. Thus, the reduction of  $E_{\text{gap}}$  is directly proportional to the concentration of defects in the material.

### 3.3. FE-SEM images and EDXS spectrum for surface and chemical analysis

Fig. 3(a–c) show the low, medium, and high magnification FE-SEM images and Fig. 3(d) EDXS spectrum for spindle-like  $\text{CaWO}_4$  microcrystals, respectively.

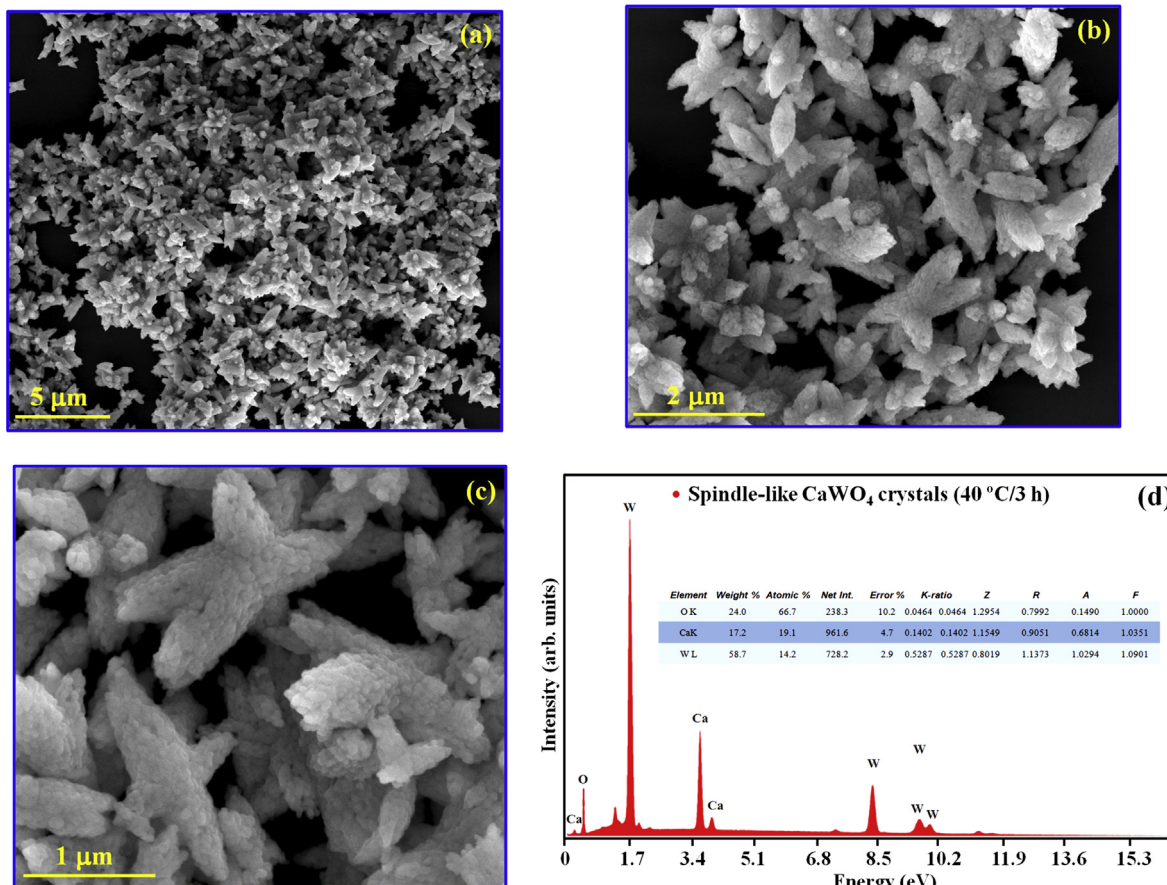


**Fig. 3.** (a) FE-SEM image at (a) low magnification (10,000×), (b) medium magnification (40,000×), (c) medium magnification (80,000×), and (d) EDXS spectrum of several spindle-like CaWO<sub>4</sub> microcrystals, respectively.

The FE-SEM images illustrated in Fig. 3(a) indicate the presence of several CaWO<sub>4</sub> microcrystals with an agglomerate nature, polydisperse shape, in which the large majority is composed of spindle-like CaWO<sub>4</sub> microcrystals. These images also suggest that these microcrystals are formed by a large quantity of small flake-like nanocrystals, resulting from the growing quickly in an aqueous solution after the sonication and fast precipitation reaction as shown in Fig. 3(b and c). Moreover, some of these spindle-like CaWO<sub>4</sub> microcrystals grow by means of the self-aggregation process to the formation of the star-like CaWO<sub>4</sub> microcrystals and subsequent growth of these crystals leads to the growing of flower-like CaWO<sub>4</sub> microcrystals [44]. Therefore, these FE-SEM image suggests that the flower-like CaWO<sub>4</sub> microcrystals are formed by an aggregate of spindles-like rods by means of self-assembled in a radial form similar to that proposed in the literature [42]. The large majority of our CaWO<sub>4</sub> microcrystals present the shape of the irregular spindle with an average size distribution in the range from 1.5 to 3.1 μm and an average size of 2.18 μm. While several CaWO<sub>4</sub> nanocrystals aggregated by selfassembly reveal an average size distribution being in the range from 14 to 30 nm with an average size of 21.7 nm (*Supplementary data Figs. SD-2(a,b)*). Finally, Fig. 3(d) shows an EDXS spectrum analysis for these spindle-like CaWO<sub>4</sub> microcrystals. This EDXS spectrum revealed that the powders are chemically composed of calcium (Ca), tungsten (W), and oxygen (O) atoms. Inset in Fig. 3(d) show the approximate values of elementary percentage composition (weight %). Therefore, this result confirms that the SC method is able to allow the formation of pure CaWO<sub>4</sub> microcrystals.

#### 3.4. Sonophotocatalytic process and electronic density map: Experimental and theoretical

Fig. 4 displays the temporal evolution of the UV–Vis absorption spectra of RhB dye solution after 200 min of illumination under UV-C light ( $\lambda = 254 \text{ nm} \approx 4.88 \text{ eV}$ ) for (a) photolysis (P) process; only with ultrasonic radiation for (b) sonolysis (S) process; under ultrasonic radiation and UV-C light for (c) sonophotolysis (SP) process; under UV-C light and CaWO<sub>4</sub> microcrystals as catalysts for (d) photocatalysis (PC) process; under ultrasonic radiation, UV-C light, and CaWO<sub>4</sub> microcrystals as catalysts for (e) sonophotocatalysis (SPC) process. Fig. 4(f) illustrates the evolutions for all the degradation rate ( $C_n/C_0$  vs. time) and the insets show kinetic ( $k$ ) constants values for all processes employed to degradation of the RhB dye solution using the CaWO<sub>4</sub> microcrystals as catalysts, respectively. Fig. 4(g and h) show the electronic density maps on the (110) plane for optimized structure and defected structure with the presence of bonds elongated in Ca–O and W–O, respectively.

As shown in Fig. 4(a), the degradation rate for the RhB dye solution was almost insignificant after 200 min by the P process (about 4% degradation), indicating a large resistance of RhB dye when it is employed only UV-C light [45]. However, when the S process is employed, we have noted a considerable improvement of ≈37% degradation of RhB dye solution, as shown in Fig. 4(b). According to the literature [46], the water sonolysis produces H<sup>+</sup> atom and hydroxyl (HO<sup>•</sup>) radicals. In other paper reported [47] has been observed through electron paramagnetic resonance spectroscopy that the production rate (molar) of HO<sup>•</sup> radicals increase with the

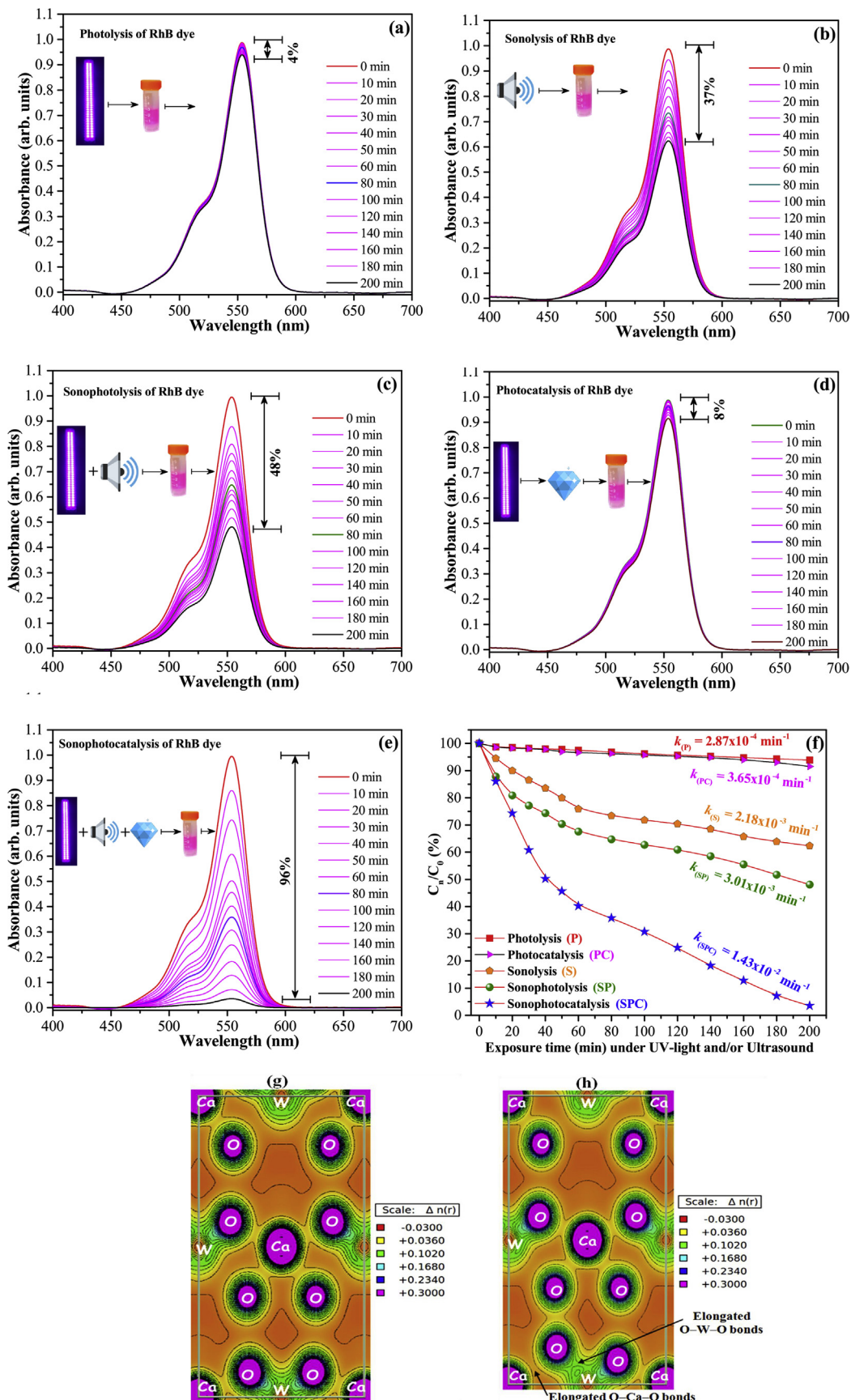


**Fig. 4.** (a–e) UV–Vis absorption spectra of RhB dye solution after 200 min of UV-C illumination/ultrasonic radiation, (f) degradation rate ( $C_n/C_0$  vs. time) and kinetics k-constants values for all processes involved with and without the CaWO<sub>4</sub> catalyst. Electronic density map for (g) optimized structure and (h) defected structure, respectively.

rise of ultrasound energy. However, the production rate (molar) of HO<sup>•</sup> radicals increases until a certain limit sonication time to each chemical reaction case. Fig. 4(c) shows an increase in the degradation rate of the RhB dye solution after 200 min by the SP process (at around 48% degradation) when ultrasound and UV-C light are used simultaneously. This behavior is due to the synergistic effect between the sonolysis and photolysis improves the sonochemistry processes and promotes the bond cleavage of water (H<sub>2</sub>O) molecules and adsorbed oxygen (O<sub>2</sub>) gases at H<sub>2</sub>O molecules causing the broken and decomposition into an H<sup>\*</sup> atom and HO<sup>•</sup> radicals and superoxide anion (O<sub>2</sub><sup>•</sup>) radicals resulting in the formation of perhydroxyl (O<sub>2</sub>H<sup>\*</sup>) radical [48]. Fig. 4(d) illustrates the PC process (about 8% degradation) when UV-C light and CaWO<sub>4</sub> microcrystals are used. According to previous investigations reported in the literature [49–52], the pure CaWO<sub>4</sub> crystals have low photocatalytic efficiency or are not able to the photodegradation of RhB dyes or other organic molecules under UV and/or Vis light. As displayed in Fig. 4(e), a high degradation rate at around 96% is achieved when the SPC process is employed. We attribute this considerable improvement in the catalytic properties to the beneficial and synergic effect of ultrasonic radiation and UV-light allow to activation of active sites of our CaWO<sub>4</sub> catalysts and the rise of the amount of H<sup>\*</sup> atom, HO<sup>•</sup> radicals at VB and O<sub>2</sub><sup>•</sup> radicals at CB are more available, which allows a good catalytic performance to the CaWO<sub>4</sub> microcrystals, not yet reported in the literature. Therefore, we present in Tables SD–2 a comparative of photocatalysis and sonophotocatalysis properties obtained in this work, with those reported in the literature for CaWO<sub>4</sub> crystals synthesized by other methods (Supplementary data Tables SD–2).

The ultrasound facilitates the transport of RhB dye molecules to the surface of the CaWO<sub>4</sub> catalyst microcrystals, where it can absorb, and react with the OH<sup>•</sup> radicals generated by the reaction of holes (h<sup>•</sup>) with adsorbed H<sub>2</sub>O molecules. Moreover, the microconvection may also assist desorption of the product from the catalyst surface, making it accessible to the next RhB dye molecules, prevent the agglomeration of catalyst CaWO<sub>4</sub> microcrystals and still increase the effective surface area of these particles, with the consequent increase in the extent of adsorption of RhB dye molecules [53,54].

According to the previous works [55,56], a high photodegradation rate for RhB dye or cationic dyes can be achieved using visible/irradiation light, activated carbon bimetallic nanocomposite, presence of hydrogen peroxide (H<sub>2</sub>O<sub>2</sub>) and scavengers, such as dimethyl sulphoxide (DMSO), benzoquinone (BQ), triethanolamine (TEOA) and potassium dichromate (PD).

To quantitatively understand the reaction kinetics for the discoloration of the RhB dye by the CaWO<sub>4</sub> catalyst microcrystals, as illustrated in Fig. 4(f), we applied the pseudo-first order model expressed in equation (2) to obtain the rate constants (*k*):

$$-\ln\left(\frac{C_n}{C_0}\right) = kt \quad (2)$$

where C<sub>0</sub> and C<sub>n</sub>(%) is the initial and different concentration of the dye solution of UV-C illumination, *t* is the exposure time, and *k* is the pseudo-first-order rate constant. This equation is generally used for a P, S, SP, PC, and SPC processes if the initial concentration of the pollutant is low (1 × 10<sup>-5</sup> mol L<sup>-1</sup>). According to equation (2), a plot of [-ln(C<sub>n</sub>/C<sub>0</sub>)] as a function of *t* gives a straight line where the slope is *k*. The results obtained by the equation (2) for the *k* values for each process using our CaWO<sub>4</sub> catalyst microcrystals are illustrated in Fig. 4(f). As it can be noted in the insets Fig. 4(f) the SPC process is more effective for the degradation of RhB dye. Moreover, the rate constants values for the degradation of RhB dye

presents a following ascending order: *k*<sub>(P)</sub> = 2.87 × 10<sup>-4</sup> min<sup>-1</sup> < *k*<sub>(PC)</sub> = 3.65 × 10<sup>-4</sup> min<sup>-1</sup> < *k*<sub>(S)</sub> = 2.18 × 10<sup>-3</sup> min<sup>-1</sup> < *k*<sub>(SP)</sub> = 3.01 × 10<sup>-3</sup> min<sup>-1</sup> < *k*<sub>(SPC)</sub> = 1.43 × 10<sup>-2</sup> min<sup>-1</sup>). Therefore, we attributed that the synergistic effect of ultrasound radiation and UV-C light promotes the activation of catalytic sites favoring the formation of more H<sup>\*</sup> atom, HO<sup>•</sup> radicals at VB, and O<sub>2</sub><sup>•</sup> radicals at CB, which are necessary for the degradation of the RhB dye in aqueous solution. Finally, Fig. 4(g and h) displays the electronic density map on the Ca, W, and O atoms in the (110) plane for the optimized and defected structure. On the optimized structure (Fig. 4(g)), a homogeneous electron and charge distribution between the atoms of the [CaO<sub>8</sub>] and [WO<sub>4</sub>] clusters are observed and the isolines demonstrated that the bonds between the atoms are of the covalent type. However, with the bond elongated in the Ca–O and W–O caused by the defect in the O atom, inhomogeneous electron and charges distribution in this region are observed instead (Fig. 4(h)). The covalent character of the Ca–O bond is lost and becomes an ionic bond, while the W–O continues with a covalent character but weaker due to the bond elongated.

#### 4. Conclusions

In summary, spindle-like CaWO<sub>4</sub> microcrystals were successfully synthesized by the SC method at 40 °C for 3 h. XRD patterns, micro-Raman, FT-IR and EDXS spectra confirmed that our CaWO<sub>4</sub> microcrystals are monophasic with scheelite-type tetragonal structure. The Raman-active and IR-active modes proved the existence of local order at a short-range for our CaWO<sub>4</sub> microcrystals. Moreover, the relative positions of experimental Raman and IR-active modes were corroborated with those theoretically calculated by the DFT method. FE-SEM images revealed that the CaWO<sub>4</sub> microcrystals with spindles-like morphologies have an average crystals size of 2.18 μm and these CaWO<sub>4</sub> nanocrystals aggregated by self-assembly presents an average crystals size 21.7 nm, respectively. The experimental optical band gap E<sub>gap(exp)</sub> was found to be 4.69 eV with the possible existence of intermediary energy states within the band gap. The theoretical calculation indicated that the EBS of CaWO<sub>4</sub> microcrystals is characterized by direct electronic transitions, with an E<sub>gap(theo)</sub> equal a 5.70 eV to optimized structure, while the defected structure presents an E<sub>gap(theo)</sub> equal a 4.29 eV where is much closer to E<sub>gap(exp)</sub> value, demonstrating that the band gap value is related to the order/disorder of the material and a decrease of this value is due to the presence of intermediate energy levels between the gap region (VB and CB). According to the DOS analyses, the energy states in the VB is constituted mainly from O 2p orbitals, while in the CB has a major contribution related to (W 5d) orbitals. When is provoked a local defect in the O atom, it's noted that affects both VB and CB which is referent to the structural defect model due to the presence of new intermediate energy levels between these bands. From the electronic density map, it is possible to affirm that the local defects, such as a bond elongated, causes an inhomogeneous distribution of the electronic density and charge between the [CaO<sub>8</sub>] and [WO<sub>4</sub>] clusters, that is related to the capacity of the material to generate electron and holes pairs. Finally, the SPC process using CaWO<sub>4</sub> catalyst microcrystals was more promising than the traditional PC process, due to the synergistic effect between ultrasound radiation and UV-C light to unblocking the active catalytic sites, assist desorption of the product from the catalyst surface and promoting the formation of more H<sup>\*</sup> atom, HO<sup>•</sup> radicals at VB and O<sub>2</sub><sup>•</sup> radicals, which are necessary conditions for the high degradation of almost 96% RhB dye until 200 min.

## Supporting Information

Supporting Information is available online.

## Declaration of competing interest

The authors declare that they have no known competing financial interests or personal relationships that could have appeared to influence the work reported in this paper.

## Acknowledgements

The authors acknowledge the financial support of the Brazilian research financing institutions: CNPq (479644/2012-8 and 304531/2013-8), FAPESP (2019/01732-1, 2016/23891-6, and 2013/07296-2), and CAPES-PNPD (1268069).

## Appendix A. Supplementary data

Supplementary data to this article can be found online at <https://doi.org/10.1016/j.jallcom.2020.157377>.

## References

- [1] R. Chai, Y. Liu, G. Zhang, J. Feng, Q. Kang, In situ preparation and luminescence properties of  $\text{CaWO}_4$  and  $\text{CaWO}_4:\text{Ln}$  ( $\text{Ln}=\text{Eu}^{3+}$ ,  $\text{Tb}^{3+}$ ) nanoparticles and transparent  $\text{CaWO}_4:\text{Ln}/\text{PMMA}$  Nanocomposites, *J. Lumin.* 202 (2018) 65–70.
- [2] S. Yekta, M. Sadeghi, E. Babanezhad, Synthesis of  $\text{CaWO}_4$  nanoparticles and its application for the adsorption-degradation of organophosphorus cyanophosphates, *J. Water Process Eng.* 14 (2016) 19–27.
- [3] N.A. Sabu, K.P. Priyanka, S. Ganesh, T. Varghese, Modifications in the structural and optical properties of nanocrystalline  $\text{CaWO}_4$  induced by 8 MeV electron beam irradiation, *Radiat. Phys. Chem.* 123 (2016) 1–5.
- [4] N. Faure, C. Borel, M. Couchaud, G. Basset, R. Templier, C. Wyon, Optical properties and laser performance of neodymium doped scheelites  $\text{CaWO}_4$  and  $\text{NaGd(WO}_4)_2$ , *Appl. Phys. B* 63 (1996) 593–598.
- [5] V.B. Mikhailik, I.K. Baillif, H. Kraus, P.A. Rodnyi, J. Ninkovic, Two-photon excitation and luminescence of a  $\text{CaWO}_4$  scintillator, *Radiat. Meas.* 38 (2004) 585–588.
- [6] Z. Hou, C. Li, J. Yang, H. Lian, P. Yang, R. Chai, Z. Cheng, J. Lin, One-dimensional  $\text{CaWO}_4$  and  $\text{CaWO}_4:\text{Tb}^{3+}$  nanowires and nanotubes: electrospinning preparation and luminescent properties, *J. Mater. Chem.* 19 (2009) 2737–2746.
- [7] B. Tian, M. Wang, C. Liu, S. Liu, L. Jin, X. Yan, C. Li, Z. Wang, Luminescent hollow  $\text{CaWO}_4$  microspheres: template-free synthesis, characterization and application in drug delivery, *RSC Adv.* 5 (2015) 104172–104178.
- [8] L. Li, F. Qin, L. Li, H. Gao, Z. Zhang, Optical temperature sensing with  $\text{CaWO}_4:\text{Yb}^{3+}/\text{Er}^{3+}$  phosphors driven by a 405 nm laser diode, *Optic Commun.* 452 (2019) 463–466.
- [9] A. Sahmi, K. Bensadok, M. Trari, Photoelectrochemical properties of  $\text{CaWO}_4$  synthesized by chemical route. Application to the phenobarbital electro-photocatalysis, *J. Photochem. Photobiol. A* 349 (2017) 36–41.
- [10] A. Taoufyq, V. Mauroy, T. Fiorido, F. Guinneton, J.-C. Valmalette, B. Bakiz, A. Benlhachemi, A. Lyoussi, G. Nolibe, J.-R. Gavarri, Photoluminescence properties of  $\text{CaWO}_4$  and  $\text{CdWO}_4$  thin films deposited on  $\text{SiO}_2/\text{Si}$  substrates, *J. Lumin.* 215 (2019), 116619–9.
- [11] S.P. Culver, R.L. Brutcher, Lanthanide-activated scheelite nanocrystal phosphors prepared by the low-temperature vapor diffusion sol – gel method, *Dalton Trans.* 45 (2016) 18069–18073.
- [12] R. Polini, B. Paci, A. Generosi, G. Marcheselli, Synthesis of scheelite nanoparticles by mechanically assisted solid-state reaction of wolframite and calcium carbonate, *Miner. Eng.* 138 (2019) 133–138.
- [13] K. Somasundaram, C.K. Rastogi, I. Roy, P.C. Selvin, V. Sudarsan, Lanthanide ion induced phase decomposition of tetragonal  $\text{CaWO}_4$ , *Mater. Res. Bull.* 113 (2019) 133–140.
- [14] F.M. Pontes, M.S. Galhiane, L.S. Santos, L.A. Petit, F.P. Kataoka, G.H. Mabuchi, E. Longo, M. Zampieri, P.S. Pizani, Polymeric precursor method to the synthesis of  $\text{XWO}_4$  ( $\text{X} = \text{Ca}$  and  $\text{Sr}$ ) thin films—structural, microstructural and spectroscopic investigations, *J. Alloys Compd.* 477 (2009) 608–615.
- [15] T.J. Boyle, P. Yang, K. Hattar, B.A. Hernandez-Sanchez, M.L. Neville, S. Hoppe, Synthesis and characterization of solvothermal processed calcium tungstate nanomaterials from alkoxide precursors, *Chem. Mater.* 26 (2014) 965–975.
- [16] Q. Li, Y. Shen, T. Li, Fast microwave-assisted synthesis and photoluminescence of  $\text{CaWO}_4$  nanocrystals, *J. Chem.* 2013 (2013) 952954–952961.
- [17] J.H. Ryu, S.Y. Bang, J.-W. Yoon, C.S. Lim, K.B. Shim, Pulsed laser induced synthesis of scheelite-type colloidal nanoparticles in liquid and the size distribution by nanoparticle tracking analysis, *Appl. Surf. Sci.* 253 (2007) 8408–8414.
- [18] Y. Zhang, A. Abraha, R. Zhang, T. Shahbazyan, M. Fadavi, E. Heydari, Q. Dai, Luminescence properties of  $\text{CaWO}_4$  and  $\text{CaWO}_4:\text{Eu}^{3+}$  nanostructures prepared at low temperature, *Opt. Mater.* 84 (2018) 115–122.
- [19] M. Zargazi, M.H. Entezari, Sonochemical versus hydrothermal synthesis of bismuth tungstate nanostructures: photocatalytic, sonocatalytic and sono-photocatalytic activities, *Ultrason. Sonochem.* 51 (2019) 1–11.
- [20] A. Sobhani-Nasab, H. Naderi, M. Rahimi-Nasrabadi, M.R. Ganjali, Evaluation of supercapacitive behavior of samarium tungstate nanoparticles synthesized via sonochemical method, *J. Mater. Sci. Mater. Electron.* 28 (2017) 8588–8595.
- [21] R. Talebi, Simple sonochemical synthesis and characterization of nickel tungstate nanoparticles and its photocatalyst application, *J. Mater. Sci. Mater. Electron.* 27 (2016) 3565–3569.
- [22] D.H. Bremner, A.E. Burgess, R. Chand, The chemistry of ultrasonic degradation of organic compounds, *Curr. Org. Chem.* 15 (2011) 168–177.
- [23] R. Dovesi, A. Erba, R. Orlando, C.M. Zicovich-Wilson, B. Civalleri, L. Maschio, M. Rerat, S. Casassa, J. Baima, S. Salustro, B. Kirtman, *WIREs Comput. Mol. Sci.* 8 (2018) e1360, e1361–36.
- [24] R. Dovesi, V.R. Saunders, C. Roetti, R. Orlando, C.M. Zicovich-Wilson, F. Pascale, B. Civalleri, K. Doll, N.M. Harrison, I.J. Bush, P. D'Arco, M. Ilunell, M. Causà, Y. Noël, L. Maschio, A. Erba, M. Rerat, S. Casassa, CRYSTAL17 User's Manual, University of Torino, Torino, 2017.
- [25] A.D. Becke, Density-functional thermochemistry. I. The effect of the exchange-only gradient correction, *J. Chem. Phys.* 96 (1992) 2155–2160.
- [26] A.D. Becke, Density functional thermochemistry. III. The role of exact exchange, *J. Chem. Phys.* 98 (1996) 5648–5652.
- [27] R.M. Hazen, L.W. Finger, J.W.E. Mariathasan, High-pressure crystal chemistry of scheelite-type tungstates and molybdates, *J. Phys. Chem. Solid.* 46 (1985) 253–263.
- [28] I.C. Nogueira, L.S. Cavalcante, P.F.S. Pereira, M.M. de Jesus, J.M.R. Mercury, N.C. Batista, M.S. Li, E. Longo, Rietveld refinement, morphology and optical properties of  $(\text{Ba}_{1-x}\text{Sr}_x)\text{MoO}_4$  crystals, *J. Appl. Crystallogr.* 46 (2013) 1434–1446.
- [29] L.S. Cavalcante, V.M. Longo, J.C. Sczancoski, M.A.P. Almeida, A.A. Batista, J.A. Varela, M.O. Orlandi, E. Longo, M.S. Li, Electronic structure, growth mechanism and photoluminescence of  $\text{CaWO}_4$  crystals, *CrystEngComm* 14 (2012) 853–868.
- [30] N. Khobragade, E. Sinha, S.K. Rout, M. Kar, Structural, optical and microwave dielectric properties of  $\text{Sr}_{1-x}\text{Ca}_x\text{WO}_4$  ceramics prepared by the solid state reaction route, *Ceram. Int.* 39 (2013) 9627–9635.
- [31] T. Thongtem, S. Kungwankunkorn, B. Kuntalue, A. Phuruangrat, S. Thongtem, Luminescence and absorbance of highly crystalline  $\text{CaMoO}_4$ ,  $\text{SrMoO}_4$ ,  $\text{CaWO}_4$  and  $\text{SrWO}_4$  nanoparticles synthesized by co-precipitation method at room temperature, *J. Alloys Compd.* 506 (2010) 475–481.
- [32] P. Kubelka, F. Munk, Ein Beitrag zur optik der farbanstriche, *Z. Tech. Phys.* 12 (1931) 593–601.
- [33] P.F.S. Pereira, I.C. Nogueira, E. Longo, E.J. Nassar, I.L.V. Rosa, L.S. Cavalcante, Rietveld refinement and optical properties of  $\text{SrWO}_4:\text{Eu}^{3+}$  powders prepared by the non-hydrolytic sol-gel method, *J. Rare Earths* 33 (2015) 113–128.
- [34] I.P. Carvalho, A.F. Lima, M.V. Lalic, Theoretical study of electronic and optical properties of the scheelite  $\text{MWO}_4$  ( $\text{M} = \text{Ca}, \text{Sr}$  or  $\text{Ba}$ ) compounds by applying the modified Becke-Johnson exchange-correlation potential, *Opt. Mater.* 92 (2019) 187–194.
- [35] R. LaComba-Perales, J. Ruiz-Fuentes, D. Errandonea, D. Martínez-García, A. Segura, Optical absorption of divalent metal tungstates: correlation between the band-gap energy and the cation ionic radius, *Europhys. Lett.* 83 (2008) 37002–37006.
- [36] R. LaComba-Perales, D. Errandonea, A. Segura, J. Ruiz-Fuentes, P. Rodríguez-Hernández, S. Radescu, J. López-Solano, A. Mujica, A. Muñoz, A combined high-pressure experimental and theoretical study of the electronic band-structure of scheelite-type  $\text{AVO}_4$  ( $\text{A}=\text{Ca}, \text{Sr}, \text{Ba}, \text{Pb}$ ) compounds, *J. Appl. Phys.* 110 (2011) 43703–43708.
- [37] V.M. Longo, E. Orhan, L.S. Cavalcante, S.I. Porto, J.W.M. Espinosa, J.A. Varela, E. Longo, Understanding the origin of photoluminescence in disordered  $\text{Ca}_{0.60}\text{Sr}_{0.40}\text{WO}_4$ : an experimental and first-principles study, *Chem. Phys.* 334 (2007) 180–188.
- [38] R.F. Gonçalves, L.S. Cavalcante, I.C. Nogueira, E. Longo, M.J. Godinho, J.C. Sczancoski, V.R. Mastelaro, I.M. Pinatti, I.L.V. Rosa, A.P.A. Marques, Rietveld refinement, cluster modelling, growth mechanism and photoluminescence properties of  $\text{CaWO}_4:\text{Eu}^{3+}$  microcrystals, *CrystEngComm* 17 (2015) 1654–1666.
- [39] Z. Shan, Y. Wang, H. Ding, F. Huang, Structure-dependent photocatalytic activities of  $\text{MWO}_4$  ( $\text{M} = \text{Ca}, \text{Sr}, \text{Ba}$ ), *J. Mol. Catal. Chem.* 302 (2009) 54–58.
- [40] O.Y. Khyzhun, T. Strunskus, S. Cramm, Y.M. Solonin, Electronic structure of  $\text{CuWO}_4$ : XPS, XES and NEXAFS studies, *J. Alloys Compd.* 389 (2005) 14–20.
- [41] O.Y. Khyzhun, V.L. Bekenev, Y.M. Solonin, First-principles calculations and X-ray spectroscopy studies of the electronic structure of  $\text{CuWO}_4$ , *J. Alloys Compd.* 480 (2009) 184–189.
- [42] S. Rajagopal, V.L. Bekenev, D. Nataraj, D. Mangalaraj, O. Yu Khyzhun, Electronic structure of  $\text{FeWO}_4$  and  $\text{CoWO}_4$  tungstates: first-principles FP-LAPW calculations and X-ray spectroscopy studies, *J. Alloys Compd.* 496 (2010) 61–68.
- [43] O.Y. Khyzhun, V.L. Bekenev, V.V. Atuchin, E.N. Galashov, V.N. Shlegel, Electronic properties of  $\text{ZnWO}_4$  based on ab initio FP-LAPW band-structure calculations and X-ray spectroscopy data, *Mater. Chem. Phys.* 140 (2013) 588–595.

- [44] L. Yang, Y. Wang, Y. Wang, X. Wang, G. Han, Shape-controlled of CaWO<sub>4</sub> microcrystals by self-assembly of nanocrystals via a simple sonochemical method, *Adv. Powder Technol.* 24 (2013) 721–726.
- [45] Y. Zhang, R. Fan, Q. Zhang, Y. Chen, O. Sharifi, D. Leszczynska, R. Zhang, Q. Dai, Synthesis of CaWO<sub>4</sub>-biochar nanocomposites for organic dye removal, *Mater. Res. Bull.* 110 (2019) 169–173.
- [46] K. Makino, M.M. Mossoba, P. Riesz, Chemical effects of ultrasound on aqueous solutions. Formation of hydroxyl radicals and hydrogen atoms, *J. Phys. Chem.* 87 (1983) 1369–1377.
- [47] H. Yanagida, Y. Masubuchi, K. Minagawa, T. Ogata, J.-I. Takimoto, K. Koyama, A reaction kinetics model of water sonolysis in the presence of a spin-trap, *Ultrason. Sonochem.* 5 (1999) 133–139.
- [48] P. Sathishkumar, R.V. Mangalaraja, S. Anandan, Review on the recent improvements in sonochemical and combined sonochemical oxidation processes – a powerful tool for destruction of environmental contaminants, *Renew. Sustain. Energy Rev.* 55 (2016) 426–454.
- [49] Z. Zhang, W. Wang, D. Jiang, J. Xu, Synthesis of dumbbell-like Bi<sub>2</sub>WO<sub>6</sub>@CaWO<sub>4</sub> composite photocatalyst and application in water treatment, *Appl. Surf. Sci.* 292 (2014) 948–953.
- [50] Y. Guo, G. Zhang, H. Gan, Y. Zhang, Micro/nano-structured CaWO<sub>4</sub>/Bi<sub>2</sub>WO<sub>6</sub> composite: synthesis, characterization and photocatalytic properties for degradation of organic contaminants, *Dalton Trans.* 41 (2012) 12697–12703.
- [51] A. Vosoughifar, Photodegradation of dye in waste water using CaWO<sub>4</sub>/NiO nanocomposites; Co-precipitation preparation and characterization, *J. Mater. Sci. Mater. Electron.* 29 (2018) 3194–3200.
- [52] Z. Shan, Y. Wang, H. Ding, F. Huang, Structure-dependent photocatalytic activities of MWO<sub>4</sub> (M = Ca, Sr, Ba), *J. Mol. Catal. Chem.* 302 (2009) 54–58.
- [53] A.A. Zewde, L. Zhang, Z. Li, E.A. Odey, A review of the application of sono-photocatalytic process based on advanced oxidation process for degrading organic dye, *Rev. Environ. Health* 34 (2019) 365–375.
- [54] C. Balaji, V.S. Moholkar, A.B. Pandit, M. Ashokkumar, Mechanistic investigations on sonophotocatalytic degradation of textile dyes with surface active solutes, *Ind. Eng. Chem. Res.* 50 (2011) 11485–11494.
- [55] G. Sharma, D.D. Dionysiou, S. Sharma, A. Kumar, A.H. Al-Muhtaseb, M. Naushad, F.J. Stadler, Highly efficient Sr/Ce/activated carbon bimetallic nanocomposite for photoinduced degradation of rhodamine B, *Catal. Today* 335 (2019) 437–451.
- [56] G. Sharma, A. Kumar, S. Sharma, M. Naushad, T. Ahamad, A.H. Al-Muhtaseb, M. Naushad, F.J. Stadler, S.I. Al-Saeedi, G.M. Al-Senani, N.S. Al-kadhi, F.J. Stadler, Facile fabrication of Zr<sub>2</sub>Ni<sub>1</sub>Cu<sub>7</sub> trimetallic nano-alloy and its composite with Si<sub>3</sub>N<sub>4</sub> for visible light assisted photodegradation of methylene blue, *J. Mol. Liq.* 272 (2018) 170–179.